2.5D crosshole GPR full-waveform inversion with synthetic and measured data

Amirpasha Mozaffari[1,2] (a.mozaffari@fz-juelich.de), Anja Klotzsche[1,2] (a.klotzsche@fz-juelich.de), Craig Warren[3] (craig.warren@northumbria.ac.uk), Guowei He[1,2] (g.he@fz-juelich.de), Antonios Giannopoulos[4] (A.Giannopoulos@ed.ac.uk), Harry Vereecken[1,2] (h.vereecken@fz-juelich.de), Jan van der Kruk[1,2] (j.van.der.kruk@fz-juelich.de)

[1] Agrosphere (IBG-3), Institute of Bio- and Geosciences, Forschungszentrum Jülich GmbH, Germany

[2] Centre for High-Performance Scientific Computing in Terrestrial Systems (TerrSys), Geoverbund ABC/Jülich, Germany

[3] Department of Mechanical and Construction Engineering, Northumbria University, Newcastle upon Tyne, United Kingdom

[4] Institute for Infrastructure and Environment, School of Engineering, The University of Edinburgh, Edinburgh, United Kingdom

Running Head: 2.5D GPR full-waveform inversion

Corresponding author: Amirpasha Mozaffari

Abstract

Full-waveform inversion (FWI) of cross-borehole Ground Penetrating Radar (GPR) data is a technique with the potential to investigate the subsurface structures. Typical FWI applications transform the 3D measurements into a 2D domain via an asymptotic 3D to 2D data transformation, widely known as a *Bleistein filter*. Despite the broad use of such a transformation, it requires some assumptions that make it prone to errors. Although the existence of the errors is known, previous studies have failed to quantify the inaccuracies introduced on permittivity and electrical conductivity estimation. Based on a comparison of 3D and 2D modeling, errors could reach up to 30% of the original amplitudes in layered structures with high contrast zones. These inaccuracies can significantly affect the performance of the crosshole GPR FWI in estimating permittivity and especially electrical conductivity. We addressed these potential inaccuracies by introducing a novel 2.5D crosshole GPR FWI that utilizes a 3D finite-difference time-domain forward solver (gprMax3D). This allows us to model GPR data in 3D, while carrying out FWI in the 2D plane. Synthetic results showed that 2.5D crosshole GPR FWI outperformed the 2D FWI by achieving higher resolution and lower average errors for permittivity and conductivity models. The average model errors in the whole domain were reduced by around 2% for both permittivity and conductivity, while zone-specific errors in high contrast layers were reduced by about 20%. We verified our approach using crosshole 2.5D FWI measured data, and the results showed good agreement with previous 2D FWI results and geological studies. Moreover, we analyzed various approaches and found an adequate trade-off between computational complexity and accuracy of the results, i.e. reducing the computational effort whilst maintaining the superior performance of our 2.5D FWI scheme.

Key words: *Ground penetrating radar, Waveform inversion, Numerical modelling, Wave propagation*

Main Body

INTRODUCTION

Crosshole Ground Penetrating Radar (GPR) has gained popularity amongst geophysical methods for high resolution tomography of the near surface in a wide field of applications in last three decades (Hubbard et al., 1997; Slater et al., 1997; Tronicke and Holliger, 2004; Looms et al., 2008; Doetsch et al., 2010; Dorn et al., 2011). Traditionally, travel times from crosshole GPR data are used to estimate the velocity of the electromagnetic waves between the boreholes, where the velocity in the medium is inversely proportional to the relative permittivity ε_r (Annan, 2009). Amplitudes from first arrival picks can be processed to estimate the attenuation of the electromagnetic waves, where the attenuation is associated with the electrical conductivity σ of the medium. A standard approach to derive tomographic images of the subsurface is to apply a ray-based inversion (RBI) that only considers the first arrivals of the waves and corresponding first cycle amplitudes, which are a relativity small fraction of the information contained in the recorded traces (Holliger et al., 2001; Holliger and Maurer, 2004). Moreover, the resolution of the RBI tomogram is scaled by the first Fresnel zone $\sqrt{\lambda L}$, where λ is wavelength and L is the total path. Therefore, RBI is mostly reliable for models that have a small variation of medium properties relative to the wavelength, and struggles with presence of high contrast layers (Stratton, 2015; Williamson, 1991; Rector and Washbourne, 1994; Brenders and Pratt, 2007).

Tarantola (1984) was one of the first who introduced the high-fidelity data fitting technique for seismic data known as full-waveform inversion (FWI). In contrast to RBI, FWI includes the entire waveform (or at least the first few cycles) of the signal, and its resolution approaches half of the dominant wavelength or better. As a rule of thumb, by moving from RBI to FWI, the spatial resolution can improve by up to one order of magnitude for and for borehole applications, it can reach to one of borehole logging methods (Wu and Toksöz, 1987; Dickens, 1994; Pratt and Shipp, 1999; Dessa and Pascal, 2003; Belina et al., 2009; Virieux and Operto, 2009; Warner et al., 2013). Since the pioneering work by Tarantola (1984), a large number of FWI approaches for acoustic and elastic waves have been proposed using time-domain, frequency-domain, and hybrid methods (Sirgue et al., 2008; Butzer et al., 2013; Lavoué et al., 2013; Warner et al., 2013; Agudo et al., 2016). Despite the existence of an elastic solution for crosshole seismic FWI, many applications are still restricted to acoustic-wave solutions due to the high computational costs of both the forward modeling and inversion (Pratt et al., 1998; Hollender et al., 1999; Ernst et al., 2007a; Butzer et al., 2013). Within the last decade, FWI was adapted for electromagnetic wave propagation, especially for crosshole GPR (detailed overview by Klotzsche et al., 2019). Because finite-difference solutions of Maxwell's equations are computationally comparable to those of the viscoacoustic-wave equations in seismic, most of the applications of GPR FWI used a 2D FDTD forward modeling (Ernst et al., 2007a; Meles et al., 2010). Kuroda et al. (2007) introduced a time-domain 2D FWI to obtain ε_r by performing synthetic studies. Ernst et al. (2007a, 2007b) developed a 2D FWI that utilize a gradient-based method to obtain high resolution ε_r and σ tomograms, and applied it to synthetic and experimental data. Meles et al. (2010) extended the approach of Ernst et al. (2007a) by incorporating the vector-based properties of the electromagnetic fields into the FWI, and simultaneously updating ε_r and σ. Next to the time-domain approaches, several frequency-domain FWI approaches have been developed in the last few years. For example, Lavoué et al. (2014) proposed a frequency-domain 2D FWI that could reconstruct the ε_r and σ of multi-offset GPR for a synthetic model.

The first application of 2D crosshole GPR FWI to experimental data based on Meles et al. (2010) was performed by Klotzsche et al. (2010). Since this initial application, FWI has been continuously developed to enhance the application to experimental data and multiple field applications have been conducted, including the characterization of aquifers (Klotzsche et al., 2013; Gueting et al., 2017), karst (Keskinen et al., 2017), and clayey till (Looms et al., 2018). Studies related to the Widen site (Klotzsche et al., 2013) and the Boise hydrogeophysical test site (Klotzsche et al., 2014) specifically indicated the potential of FWI to obtain high-resolution subsurface images including high-contrast layers that were not able to be detected by RBI. Such layers are important to accurately map and detect, because they can be linked to hydrologically relevant features such as high porosity zones, preferential flow paths, and impermeable clay lenses that can significantly effect to flow and transport characteristic of aquifers. High resolution 2D forward modeling demonstrates that such high contrast layers, related to an increased ε_r, can act as low-velocity waveguides causing late arrival high amplitude events in the data. An overview of the current state-of-the-art of crosshole GPR FWI and its application to experimental data is provided by Klotzsche et al. (2019).

All of the applications of crosshole GPR FWI to experimental data were carried out with a computationally attractive 2D forward model. FWI using a complete 3D model with realistic model size requires significantly higher computational resources and large memory requirements. Wave propagation in 2D and 3D media have differences in its geometrical spreading, phase, and frequency scaling characteristics. It is necessary to take these differences into account before using a 2D forward model to invert measured data obtained in a 3D environment (Ernst et al., 2007a; Brossier et al., 2009; Červený and Pšenčík, 2011; Watson, 2016). The normally applied 2D assumptions are valid as long as there is no out-plane arrival in the data and in the far-field regime. Any numerical or analytical solution for the 2D wave equation inherently carries the assumption that any source is a line source, i.e., that it extends infinitely out-of-plane, causing a cylindrical wave front expanding from the center line. In a 3D homogenous medium a realistic point source generates a spherical wave front. The difference in the geometrical spreading of the wave in 2D and 3D media leads to a different amplitude decay with distance r and time. In the 3D medium, the energy is spread over the surface of a sphere. Hence the amplitude is scaled with $1/r$. Whereas in the 2D environment, the energy is distributed over the surface of a cylinder, so the amplitude is scaled with $1/\sqrt{r}$. Therefore, an identical pulse will decay faster in the 3D medium. These differences in geometrical spreading also create phase differences between the 2D and 3D Green's functions. In 2D, the Green's function is scaled with $1/\sqrt{\omega}$ compared to 3D, which results in a $\pi/4$ phase shift between the wave solutions for the 3D and 2D environments (Williamson and Pratt, 1995; Červený, 2001; Miksat et al., 2008; Červený and Pšenčík, 2011). The differences in geometrical spreading in the 2D and 3D environments and the effects on the associated amplitudes and phases should be accounted for prior to the inversion. The most common practice to address this issue is to apply a 3D to 2D transformation to the field data, referred to as a "geometrical spreading correction" (Crase et al., 1990; Červený, 2001; Bleibinhaus et al., 2009; Mulder et al., 2010). The crosshole configurations restrict a transmitter and a receiver to a single plane, with the implicit assumption that there is negligible variation in the properties of the embedding medium in the direction normal to this plane (Song and Williamson, 1995). Bleistein (1986) calculated out-of-plane spreading factors using asymptotic theory and approximate asymptotic transformation for converting recorded seismic wave fields in a restricted 3D environment to two dimensions. Bleistein assumed that acoustic waves propagate in the far-field regime and that the medium properties of the host change smoothly. It is formulated in the frequency domain (where ω is the angular frequency) as:

$$\overline{G}^{2D}(\omega) = \overline{G}^{3D}(\omega)\ exp\left[\omega\left(\frac{i\pi}{4}\right)\right]\sqrt{\frac{2\pi L}{|\omega|}}, \tag{1}$$

where $\overline{G}$ is the Green's function of the 2D and 3D media. L denotes the integral of the velocity with respect to the arc-length of the ray trajectory that, in the homogeneous medium, is equal to the velocity v multiplied by the distance r between the transmitter and receiver $L = vr$. This asymptotic transformation of restricted 3D to 2D is often termed the "*Bleistein filter*" and is commonly applied in seismic data processing. Ernst et al. (2007b) adapted this transformation to electromagnetic wave propagation in the frequency domain as follows:

$$\hat{\boldsymbol{E}}^{2D}(\boldsymbol{x}_s, \boldsymbol{x}_r, \omega) = \hat{\boldsymbol{E}}^{obs}(x_s, \boldsymbol{x}_r, \omega)\sqrt{\frac{2\pi T(\boldsymbol{x}_s, \boldsymbol{x}_r)}{-i\omega\varepsilon_r^{mean}\,\mu_0}}, \tag{2}$$

where $\hat{E}^{3D}$ are the observed 3D field data and $\hat{E}^{2D}$ the transformed 2D data for each transmitter x_s and receiver x_r location, respectively. T is the travel time between the transmitter and receiver positions, $i^2 = -1$, ε_r^{mean} is the mean of the relative permittivity of the media, and μ_0 is the magnetic permeability of free space. Despite the benefits of the asymptotic 3D to 2D transformation in avoiding the requirement for computationally intensive 3D modeling, it still has some shortcomings. The transformation only uses the first-arrival times T and may perform poorly for multiple later arrivals. Auer et al. (2013) study the performance of the asymptotic transformations for seismic crosshole data and show that substantial errors are observed in data from overlapping arrivals and curved paths. These errors translate into poor model reconstruction using FWI. Ernst et al. (2007b) claimed a satisfactory performance of the asymptotic 3D to 2D transformation for experimental data in a far-field regime, but did not provide a quantitative analysis of the accuracy. Van Vorst et al. (2014) state a good performance of the asymptotic 3D to 2D transformation for GPR data for travel times, but observed high inaccuracy in the amplitude transformation that critically influenced the associated σ. Therefore, more research is required to quantify the effects of the asymptotic 3D to 2D transformation on 2D GPR FWI, and specifically investigate the electrical conductivity results in the presences of high contrast zones.

In this paper, we first present a numerical modeling study aimed at quantifying the travel time and amplitude differences between true 2D, and 3D to 2D transformed GPR crosshole data. We study the performance of the asymptotic 3D to 2D transformation in complex structures, and propose using 3D forward modeling to mitigate inaccuracies in the crosshole FWI to enhance resolution and quantify of the ε_r and σ results. Therefore, we coupled a 3D FDTD forward modeling package with our 2D FWI scheme based on Meles et al. (2010) proposing a 2.5D FWI. The performance of this novel 2.5D FWI is tested and verified using synthetic and experimental data.

EFFECTS OF THE GEOMETRICAL SPREADING CORRECTION

To quantify the influence of the asymptotic 3D to 2D transformation on the experimental data and hence the crosshole GPR FWI results, we first performed a numerical study to estimate possible errors introduced by this transformation. Previous studies (Auer et al., 2013; Van Vorst et al., 2014) indicated that the functionality of this transformation is sensitive to the degree of complexity of subsurface structures. Therefore, we designed a typical aquifer model including an unsaturated and saturated domain to study the effect of overlapping arrivals caused by the significant difference in velocity of the electromagnetic waves in unsaturated and saturated zones. Greenhalgh et al. (2007) showed that the change of acoustic wave velocity influences the performance of the asymptotic transformation more than the change in the amplitude through the interface. Because of analogous relations between visco-acoustic and electromagnetic wave propagation, the translation of this statement for electromagnetic waves is that the contrast of the ε_r values before and after the interface is more important than a change of the σ. Therefore, we limited our studies to models with variations in the ε_r and constant σ. We used a 2D FDTD (Meles et al., 2010) and a 3D FDTD (Warren et al., 2016) algorithm to compute the 2D and 3D data. Both codes use perfect matched layer (PML) boundaries (Berenger, 1994) to truncate the computational domain, and to simulate the open boundary nature of the GPR problem. Both algorithms also enforce the CFL stability condition for FDTD (Hagness and Taflove, 1997). We apply equation 2 to transform the 3D data to 2D (which we term *'semi-2D'*). The 2D model has the size 11 m x 6 m with boreholes 5 m apart located at 0.5 m and 5.5 m. The 3D model used the same dimensions as the 2D model and was extended by 1.2 m in the transverse direction with the same model parameters as the 2D plane. The numerical setup contains 11 transmitters and 65 receivers that are placed in the two opposite boreholes, from which one specific pair is located in a high contrast zone. Both models used a uniform grid with a 3 cm spatial discretization in all dimensions. Figure 1 highlights a single transmitter (no. 4) and receiver (no. 21) pair (red crosses) in four different media configurations. Models (a), (b) and (c) present water saturated scenarios, while model (d) illustrates the interaction between the unsaturated and saturated zone. Models (a) and (b) are chosen to be homogenous with ε_r values of 12 and 18, respectively. Model (c) is homogenous with a ε_r of 12 including a lateral structure with a thickness of 1 m and a ε_r of 18 located in the middle of the domain. This lateral layer acts as a low velocity waveguide that traps the emitted EM wave in this layer and causes multiple late arrival high amplitudes in the data (Klotzsche et al., 2014). Model (d) is extended from model (c) considering the unsaturated zone with a ε_r = 5. All four models have a homogenous σ with a constant value of 9.5 mS/m ($\sim 105\ \Omega m$). As source wavelet we used a predefined wavelet similar to the studies of Klotzsche et al. (2012) with a center frequency of 92 MHz for all the models.

The left column of Figure 1 shows the simplest possible ray-paths for each model, and the corresponding received waveforms are marked with the same number in the center column. The shape of the semi-2D waveform is produced by equation 2. To compare the amplitudes of the true 2D and the semi-2D waveforms, we scaled the semi-2D waveform to the maximum amplitude of 2D A_{max}^{2D} in the homogeneous cases (a) and (b), and, we use the same scaling factor for the models (c) and (d). Note the amplitude of the 3D waveforms have also been scaled for visualization purposes. It is clear that there is a good fit between the true 2D and semi-2D waveforms for the simple homogenous cases (a) and (b). The ratio of $A_{max}^{2D}/\ A_{max}^{semi-2D}$ is almost identical for models (a) and (b), despite the fact that there is a 50% difference in ε_r values of the two models. This result confirms the previous studies of Ernst et al. (2007b) and Van Vorst et al. (2014), where they claimed the good performance of the asymptotic 3D to 2D transformation for simple cases. In contrast, a significant misfit is observed between the 2D and semi-2D traces for the models (c) and (d) with a higher degree of complexity. In the model (c) multiple reflections in the waveguide structure cause later arrivals of the waves (6 ns to 12 ns). The energy distribution is also changed because the first arrival wave has less energy, and the trapped late arrival waves carry most of the energy. The misfit between the waveforms for 2D and semi-2D models (c) reaches up to 17% when waves traveling on path 1 and 2 interfere. In model (d) the misfit rises to 20% of the recorded amplitudes for waves traveling along the curved ray path (labeled 3 in Figure 1k). The maximum misfit occurs for the waves traveling along ray path 3 which overlaps with the wave traveling along ray path 2. This results in an amplitude error of 31%. For both model (c) and model (d), the error increases when the arrival of the different events overlap. It is important to note that the asymptotic 3D to 2D transformation does not provide the absolute semi-2D amplitude and therefore requires a scaling factor for homogeneous media.

The misfit in the frequency spectra increases with increasing degree of complexity of the models. These results confirm the findings of Auer et al. (2013) and Van Vorst et al. (2014), who outlined that the 3D to 2D transformation performs poorly in complex structures, where overlapping events occur, and that the transformation has a substantial influence on the amplitude of the semi-2D waveform. This problem is caused by the nature of the asymptotic 3D to 2D transformation approach that relies on the transformation of the first arrival waves and the assumption that the highest amplitude of the data is associated with this first arrival event. Therefore, the performance of the transformation for overlapping or late arrival, high amplitude events is not reliable (Klotzsche et al., 2010). Moreover, the Bleistein (1986) asymptotic transformation is based on the assumption of gradually varying medium properties. Therefore, sudden changes in medium properties, like the waveguide structure in model (c) and the transition from unsaturated to saturated zones in model (d), violate this assumption and consequently the asymptotic 3D to 2D transformation exhibits poor performance in these scenarios. It is important to point out that the asymptotic 3D to 2D transformation was initially developed to transform the acoustic waves in seismic analyses where far-field conditions almost always exist. The far-field assumption is potentially valid for the GPR crosshole setup when there is sufficient distance between the transmitter and receiver boreholes, but it is not valid for closely spaced boreholes and on-ground GPR (Streich and van der Kruk, 2007). By comparing the 2D, semi-2D, and 3D frequency spectra, we observe a small downshift in the center frequency for the semi-2D and 2D compared to the 3D. Červený and Pšenčík (2011) observed this phenomenon in seismic data, and they claimed it occurs because of differences between point and line sources. This shift is an important consideration concerning spatial resolution since the high-frequency data are necessary for detailed imaging of structures.

Summarizing, we observed poor performance of the asymptotic 3D to 2D transformation in complex structures, with amplitude mismatch errors of more than 30%. Additionally, applying the asymptotic transformation caused a loss of high-frequency content in the data, which subsequently affected the resolution of the FWI tomogram. Furthermore, Watson (2016) stated that even with the geometry of the crosshole setup limiting the transmitter and receiver to a single plane, the out-of-plane scattering is not zero. Therefore, the 2D modeling approach may not be able to resolve the data thoroughly and can lead to artifacts in the reconstruction. These shortcomings of the 3D to 2D transformation make it necessary to move towards 3D modeling for more accurate FWI. Moreover, 3D modeling makes the detailed finite-length antenna and borehole modeling possible, which could increase the accuracy of the FWI for experimental data.

NOVEL 2.5 CROSSHOLE GPR FWI METHODOLOGY

3D forward model

To reduce the issues arising from the 3D to 2D transformation, we coupled our existing 2D crosshole GPR FWI with a 3D forward modeling kernel. Therefore, we use gprMax, a well-developed software for simulating electromagnetic wave propagation based on the 3D FDTD method (Giannopoulos, 2005; Warren et al., 2016). gprMax uses PML to truncate the computational domain (Berenger, 1994; Allen Taflove, 1995; Giannopoulos, 2012) and is able to model rough surfaces and the finite-length GPR antennae (Warren and Giannopoulos, 2011). The 2D setup is extended to a 3D model , by keeping the medium properties invariant in the direction perpendicular to the plane containing the boreholes (Song and Williamson, 1995), which are cylindrical objects, producing a 2.5D model (Tabarovsky and Rabinovich, 1996).

Inverse Problem

FWI is an ill-posed problem that can solved by applying a gradient search method (Meles et al., 2010). The method requires ε_r and σ starting models with adequate initial information. Synthetic data based on these starting models need to yield results that are within half a wavelength $(\lambda/2)$ of the measured data throughout the entire domain. If the synthetic response has more than half a wavelength misfit from the measured data, the synthetic pulse could fit an earlier or later measured pulse or even skip the whole pulse. This phenomenon is called “cycle skipping”, where the inversion is trapped in a local minimum and is not able to converge to the global minima. Therefore, reasonably accurate starting models are a necessity for successful inversion (Tarantola, 1986; Chunduru et al., 1997; Virieux and Operto, 2009; Fichtner, 2011; Klotzsche et al., 2012; Warner et al., 2013). The simultaneous vector-based gradient search method minimizes the cost function C, or misfit, between the observed and modeled data using the FDTD forward model.

$$C = 0.5 \times \|\boldsymbol{E}^{syn} - \boldsymbol{E}^{obs}\|^2 \tag{3}$$

where $\boldsymbol{E}^{syn}$ and $\boldsymbol{E}^{obs}$ are the modeled and observed data for all transmitter/receiver pairs within a pre-defined time window. The gradients for the ε_r and σ are calculated by a zero-lag cross-correlation between the back propagated residual wavefield and the modeled data. These gradients define the direction that is expected to minimize the misfit function (see equation 3). In the next part, optimal step-lengths for ε_r and σ are obtained, which are used together with the gradients to simultaneously update the ε_r and σ models. Details of the calculation of the misfit function, the gradient, and the step-length can be found in Meles et al. (2010). This iterative procedure continues until the misfit between the observed and modeled data is reduced below a specified value. The method requires knowing the excitation source which is not normally the case for experimental data unknown (Pratt, 1999). Therefore, it is necessary to estimate the effective source using a deconvolution approach. For more details, see Ernst et al. (2007b) and Klotzsche et al. (2010).

CASE STUDY 1: REALISTIC SYNTHETIC MODEL

Model description and generating synthetic data

Our first case study investigates the performance of our new 2.5D FWI approach and compare the results with the standard 2D FWI. As realistic input models for the 3D forward model, we used the final 2D crosshole GPR FWI results of Klotzsche et al. (2012) that includes a high ε_r zone between 5 m to 6 m depth acting as a low-velocity waveguide (Figure 2). As discussed above, such small-scale zones cause problems in the 3D to 2D transformation by introducing possible errors especially in the full-waveform σ results. We used these models in the 3D FDTD forward solver with a known effective source wavelet to produce 3D realistic synthetic GPR data. For the model dimensions we choose a similar setup as Klotzsche et al.

(2012) with 7.62 m × 11.67 m dimensions using a cell size of 3 cm for the forward modeling and 9 cm for the inversion. We built the 3D computational grid by extending the transverse direction to 0.9 m (inversion plane in the center) and truncated the domain with 10 cells of PML at each boundary. A Hertzian dipole point source was used, and all materials were modeled as lossy dielectrics, i.e. with no frequency dispersive properties. We transformed these 3D synthetic GPR data into 2D GPR data using the standard 3D to 2D transformation. The source wavelet for the 2D FWI is updated using the deconvolution approach as proposed by Klotzsche et al. (2010). Note that this step is necessary to also account for the different radiation patters of the 3D and 2D environment. 2D FWI using the transformed data is prone to exhibit poor performance in determining ε_r and σ with a subsurface model that contains thin layers and high contrasts in medium properties. Hence, two inversions are performed: (1) 2.5 FWI using the 3D data and the known input source wavelet, and (2) 2D FWI using the asymptotic 3D to 2D data transformation and an updated source wavelet.

Starting models

Ray-based inversion can usually provide sufficient information as starting models, by using first-arrival times and first-cycle amplitudes of the data (Holliger et al., 2001; Maurer and Musil, 2004) However, Klotzsche et al. (2012) show that ray-based inversion can fail to identify the major changes in the ε_r close to high contrast regions like the water table or small-scale high contrast layers. Hence, they propose updating the starting model for the ε_r by including a homogeneous zone near the water table and water table itself. Similar to Klotzsche et al. (2012), we used the starting models based on the ray-based inversion results with an updated zone between 5 – 6 m depth. For the σ starting model we used a homogenous model similar to Klotzsche et al. (2012) that represents the mean of the first cycle amplitude inversion with a value of $\sigma = 9.5$ mS/m.

We observed that the 2.5D FWI did not converge using the same starting models as for the 2D inversion of the synthetic data, while the 2D FWI could successfully reproduce the synthetic models. We believe there were simultaneous effects from the 3D to 2D transformation that caused this issue:

- The 3D to 2D transformation shifts the data on average by 1.5 ns in time (see Figure 1). Using the 2D ray-based starting models produced data within half a wavelength for the 2D inversion. However, due to this shift, the 3D measured data are more than a half-wavelength away from the modeled data and therefore could not converge successfully due to cycle skipping.
- Because the center frequency of the transformed data using the 3D to 2D transformation is slightly lower than the original 3D data. This shift indicts that the high-frequency content in the transformed data is reduced and the transformed data have a lower spatial resolution compared to the original data. Therefore, it is easier to fit the modeled data to the transformed data with lower complexity compared to the original measured data with higher resolution. Thus, synthetic traces produced by the 2D forward model could fit the transformed data while synthetic traces from the 3D forward model could not match the original data due to the additional detail present in the 3D model.

Therefore, to guarantee an overlap within half a wavelength of the starting model based synthetic data and the measured data in the entire domain, we updated the $\boldsymbol{\varepsilon_r}$ starting model with a single homogenous upper layer with a constant value of $\varepsilon_r = 18$ in the depth range 4 m to 6 m (before in average $\varepsilon_r = 16$). This update guaranteed an overlap of half a wavelength in the entire domain and allowed successful convergence for both 2D and 2.5D FWI.

Inversion strategies

2.5D FWI requires almost 300 times more computational CPU-hours than 2D FWI due to the computationally intensive 3D modeling. As we have seen the 2.5D FWI is also more sensitive to the ε_r starting model. Hence, there is a higher chance of the inversion becoming trapped in local minima instead of converging to the global minimum. Therefore, alongside the conventional FWI (direct method), we studied possible inversion strategies that could reduce the required computational effort and increase the chance of a successful convergence (cascade method). These cascade methods require the 2D inversion to be stopped in a particular stage, and the output is used as a priori information for a new start of the inversion with more detailed starting models. Since we knew the expected output from our synthetic study, we were able to compare the performance of the 2D FWI (with asymptotic 3D to 2D transformation applied) and 2.5D FWI schemes. We quantified the evaluation by calculating the relative model error for the ε_r and σ independently as follows:

$$\xi(m_{cal})_{\sigma,\varepsilon} = 100 \times \left(\frac{m_{cal} - m_{true}}{m_{true}}\right)_{\sigma,\varepsilon} \tag{4}$$

where $\xi(m_{cal})_{\sigma,\varepsilon}$ is the relative average error (*AE*) in percentage, m_{cal} and m_{true} are the modeled and reference values for each element in the domain, respectively. As the performance of the 2D FWI is prone to inaccuracy in the layered zone, we calculated lateral average error (*LAE*) as a function of the depth alongside the *AE* in the whole domain.

Direct 2.5D FWI

The $\boldsymbol{\varepsilon_r}$ and $\boldsymbol{\sigma}$ tomograms obtained from 2D and direct 2.5D FWI strategy for identical starting model are shown in Figure 3. Comparing the results with the reference models (Figure 2) shows that both 2D and 2.5D FWI were able to qualitatively resolve the main features of the ε_r and the σ tomograms. For the ε_r tomograms, both FWIs reconstructed the three main layers successfully, while the results of the 2D FWI appear to be smoother than those from the 2.5D FWI. The σ tomograms are well-reconstructed for both approaches as both results shows main features of the synthetic input model. Despite the fact that the tomograms look similar from a qualitative perspective, a quantitative comparison shows differences in accuracy. The 2D FWI overestimates ε_r between 4.2 m - 5.7 m, where the *LAE* reaches 26%. The obtained ε_r for the 2.5D FWI fits better the reference model with a maximum *LAE* of 7% at the interface between the upper high-velocity zone and the low-velocity waveguide. The *AE* in estimated ε_r in the whole domain is 2.5% for 2D FWI, while this value is 0.18% for 2.5D FWI. The *LAE* for σ reached 32% and then dropped to -21% in the transition from high to low σ layers at depths of 5 m to 6 m. The *LAE* for the 2.5D FWI σ has maximum values of +6.5% and -21%. The *AE* for σ in the whole domain is 2.8% for 2D FWI, while this value is 0.5% for 2.5D FWI.

To evaluate the performance of the two FWI approaches with the reference model, we compare two cross-sections (A-A) and (B-B) in each model (indicated in Figure 3). The ε_r values in A-A show a better fit to the reference values for the 2.5D FWI compared to the 2D FWI (Figure 4). While both 2D and 2.5D FWI underestimate the ε_r at depths of 8 m to 10 m. The values of σ in A-A reveal a more accurate 2.5D FWI result. In the B-B cross-section, ε_r of the 2D FWI shows significant error in first 1.5 m depth and slightly misplaces the maximum peak. The ε_r values for the 2.5D FWI better fit the reference model all along cross-section B-B. The 2D FWI overestimates the σ in the upper layer and underestimates it continuously in the middle and lower areas, whereas the 2.5D FWI result was closer to the reference model. Moreover, the ε_r and σ model produced with the 2.5D FWI shows higher resolution in comparison to the results of the 2D FWI while it revealed smaller spatial variation for both ε_r and σ. This observation agrees with our hypothesis previously mentioned that the 2.5D FWI better reconstructs the 3D input models especially the electrical conductivity results by eliminating the effect of the asymptotic 3D to 2D data transformation.

The normalized root mean square (RMS) error for the 2D FWI is reduced to 22% of the initial value, while this value is reduced to 12% for 2.5D FWI results. Both 2D and 2.5D FWI had termination criteria to stop the inversion when the change of the RMS error value in two consecutive iterations was less than 0.5%. The 2D FWI stopped after 21 iterations, while the 2.5D FWI met this criterion after 23 iterations. Note that also a good data fit and no remaining gradient was present for all inversion results. Our new 2.5D FWI approach exhibits better performance over the 2D FWI in reconstructing the ε_r and σ models, regarding both correct positioning and accuracy of the assigned values. Furthermore, the ε_r and σ models of the 2.5D FWI have lower *AE* than the 2D FWI, and structures are slightly better resolved in the 2.5D FWI. Despite this superior performance, it is necessary to consider the higher computational demands of the 3D modeling used in our 2.5D FWI. Computational times for the simulations mentioned above are given in Table-1.

Cascade 2.5D FWI

As shown in Mozaffari et al. (2016), the results of the 2D FWI with a limited number of iterations can be used to improve the starting models for the 2.5D FWI, which allows a faster convergence and hence reduces the computational effort. Therefore, we applied 2D FWI to create ε_r starting models at iterations 1, 4 and 7, and then we used them for the 2.5D FWI. These ε_r models were used as starting models and were inverted with the 2.5D FWI (homogenous σ starting model) until change of the misfit between two subsequent iterations is less than 0.5% (see Figure 5). All three models successfully show the key features and structures of both ε_r and σ. Furthermore, the comparison of the ε_r and σ results show that *AE* and *LAE* are increased by using the starting models that developed for a more extended time by the 2D FWI (see Table 1), indicating an increase in inaccuracies of the tomograms.

All these results show that the percentage of the *AE* increases proportionally with increasing number of iterations of the 2D FWI used as starting models. Nevertheless, using this method could have a significant effect on the required computational effort. The computational time for the total inversion reduced by 5%, 20%, and 35% for the three models respectively, as shown in Table 1. All computations were carried out on JURECA cluster (Krause and Thörnig, 2016) , which is part of the Jülich Supercomputing Centre (JSC). It is equipped with 1872 computing nodes with two Intel Xeon (E5-2680) with 2x12 cores at 2.5 GHz, simultaneous multithreading, and DDR4 (2133 MHz) memory with various capacities from 128 to 512 GB.

2.5D FWI with updated ε_r starting model

We propose a second strategy, where we combine the methods of Klotzsche et al. (2012) and Mozaffari et al. (2016). Thereby, we update only the ε_r starting model with essential features revealed in the 2D FWI. Note that we checked for each starting model update if the half-wavelength criterion is still valid by performing forward modeling using these models and the 3D forward solver, and compared the input and the modeled data. The most significant missing attribute in the ε_r starting model that we used so far is the high ε_r layer at a depth of 5.5 m to 6.0 m. This feature is revealed after a limited number of iterations in both the 2D and 2.5D FWI, while the σ does not show significant changes. Hence, our new updated ε_r starting model consists of two-horizontal layers, where the lower and upper layer have ε_r values of 22 and 18, respectively (Figure 6a).

The 2.5D FWI with the updated ε_r starting model produced ε_r and σ tomograms with maximum *LAE* of 8% and 9%, respectively. These maximums occurred at the interface of the high ε_r layers. The *AE* for ε_r and σ errors were 0.16% and 0.45%, respectively, which is slightly better than the 2.5D FWI using the direct approach (compare Figure 6). Using this updated ε_r starting model, the 2.5D FWI required 44% less computational time to converge using the same number of CPUs. A summary of the 2D FWI and 2.5D FWI using different strategies with required computational demand is presented in Table 1. Furthermore, by comparing the convergence of the inversion and the RMS distributions over number of iterations for the different strategies (Figure 7), it can be noticed that both strategies for the 2.5D FWI result in the same final RMS value, while updating the ε_r starting model helped to reduce the RMS in earlier iterations of inversion.

In summary, despite the fact of the reduction in computational effort by using the cascaded 2.5D FWI, the final 2.5D FWI results are significantly affected by the 2D FWI drawbacks. This is because the *AE* is directly linked to the level of development of the starting model from the 2D FWI. Hence, choosing an adequate starting model based on the 2D FWI results is a compromise between the computational effort and accuracy of the results. Therefore, we do not suggest using early-stage results from the 2D FWI as an input for the 2.5D FWI. In contrast, the proposed method using a ε_r starting model for the 2.5D FWI with updates based on the results of the 2D FWI can significantly reduce the computational effort, while the accuracy of the models is not affected. We further apply this approach to invert experimental GPR data from the Widen test site.

CASE STUDY 2: EXPERIMENTAL DATA

Test site description

To validate the findings of the synthetic tests, we applied the 2.5D FWI approach to the experimental data of the Widen site (Switzerland). Several geophysical and hydrological studies have been performed at this site characterizing the aquifer in detail (Diem et al., 2010; Doetsch et al., 2010; Coscia et al., 2011). The aquifer compromises a glaciofluvial deposit that includes a 3 m alluvial loam (silty sand) at the top, a 7 m thick gravel layer, and a low permeability clay aquitard below 10 m depths (Cirpka et al., 2007). Multiple monitoring wells with 11.4 cm diameter are installed near to the river Thur. The GPR data were measured with a RAMAC Ground Vision system from Mala Geoscience with 250 MHz antennae. The dataset was acquired in neighboring boreholes on the south-west plane, where the water table was at approximately 4.2 m depth (Doetsch et al., 2010). As shown in Klotzsche et al. (2012) a high ε_r (high porosity) zone that could be linked to zones of preferential flow is located between 5 m - 6 m depth.

FWI results

We applied 2.5D FWI to the same dataset as Klotzsche et al. (2012) and used the same data pre-processing steps, except that the 3D to 2D conversion is not necessary anymore for the 2.5D FWI. The effective source wavelet was updated using the deconvolution approach for the 3D GPR data and compared to the 2D FWI effective source wavelet (Figure 8). Based on the finding of the synthetic studies, we chose as a starting model for the ε_r the updated model based on the 2D features (Figure 6a). A homogenous σ starting model of 9.5 mS/m is used. The inversion converged and the 16th iteration was estimated as an optimal solution (Figure 9), where the change of the RMS error compared to the previous iteration was less than 0.5% and no remaining gradient was present. Unfortunately, we do not have any logging data from the same boreholes. Therefore, we tried to validate the experimental based on previous studies. The ε_r and σ tomograms produced by 2.5D FWI are in a good agreement with the 2D FWI results from Klotzsche et al. (2012). The slightly upward dipping high ε_r structure between 5.3 m to 6.1 m was identified as low-velocity. We also observed the same structure using our new 2.5D FWI approach. The average σ values for 2.5D FWI results are around 1.4% lower than the average values from the 2D FWI. These differences in σ values are higher in zones with higher ε_r between 5.2 m – 6 m and 9.2 m – 10 m. The RMS misfit error between the measured and 2.5D modeled data was reduced to 50% from the starting model values. In comparison, the 2D RMS errors for the same starting model only reduced by 48%. The lower average σ in the entire domain for 2.5D FWI is the main reason for the 2% improvement in the RMS misfit compared to the 2D FWI.

The computational requirement of the 2.5D FWI is more than 300 times higher than for the 2D FWI. The small increase in accuracy of the 2.5D FWI for the experimental data is perhaps not convincing given the high computational effort. Nevertheless, higher accuracy and less uncertainty for the σ results are achieved by reducing assumptions that mainly affect the amplitudes, and hence more quantitative results are obtained. Furthermore, 3D modeling will enable us to model the borehole, borehole-filling, and realistic finite-length antennas in the future. We expect to make significant improvements in accuracy by including these features in our future simulations, which will justify the extra computational effort from using 3D forward models.

CONCLUSION

In this paper, we have investigated the performance of the asymptotic 3D to 2D transformation. Despite the usefulness of the asymptotic data transformation to avoid computationally expensive 3D modeling, it assumes that the highest wave amplitudes are associated with the first arrival. We demonstrated that this asymptotic transformation function only works accurately in such simple subsurface cases, while it fails with complex structures such as high contrast layers that produce overlapping arrivals from several different features. Moreover, the amplitudes assigned to waves after the 3D to 2D transformation are only valid for simple homogenous media and are therefore not suitable for non-uniform media. We also observed that applying the 3D to 2D transformation to measured data lowers the resolution of the data by reducing the high-frequency content. Therefore, to overcome the restrictions of the 3D to 2D conversion assumptions and to minimize the associated errors in the crosshole GPR FWI results, we extended the existing 2D FWI with a 3D forward model. Our new 2.5D FWI uses gprMax as a complete 3D FDTD modeling engine which makes the 3D to 2D transformation unnecessary. We compared the performance of 2D FWI (with 3D to 2D transformation) and the 2.5D FWI for realistic synthetic data. The results for 2.5D FWI showed higher accuracy in estimated ε_r and σ and provided lower AE in tomograms. Thereby, we observed that the ε_r starting model of the 2.5D FWI needed some modifications in comparison to the 2D starting model to still fit the requirements to provide modeled data within half of the wavelength of the measured data. The time shifts caused by the asymptotic 3D to 2D transformation placed the transformed 2D data less than the half-wavelength distance from modeled data while the original 3D data were too far from modeled data to converge. Moreover, a slight decrease in the dominant frequency of the transformed data was observed, which caused a loss of high-frequency content. Despite the lower *AE* and higher resolution of the 2.5D FWI, the trade-off is a significant increase in computational resources. Therefore, we examined multiple strategies to improve the starting model by using results from the less computationally intensive 2D FWI directly. We have studied the possibility of using the 2D FWI intermediate results as input for 2.5D FWI to reduce the required computational effort. But we found out that this method will introduce inaccuracies and we have abandoned this idea. Alternatively, we found that by updating the starting model based on the main features obtained by 2D FWI, we can reduce the computational costs by more than 40% while maintaining accuracy and resolution.

Finally, we applied the novel 2.5D FWI to previously studied experimental GPR data from the Widen test site (Switzerland) to investigate changes achieved in the final tomograms. The results showed agreement with previous 2D works, and all the expected structures were identified. As expected, the main improvement was that the σ tomogram shows higher values in zones of higher ε_r and high contrast layers. For both synthetic and experimental data, we have seen that using the ray-based results as starting models for the 2.5D FWI causes the inversion to be trapped in a local minimum and an update of the permittivity model was required to successfully perform the inversion. Overall, we demonstrated that our new 2.5D FWI with 3D forward modeling is a valuable tool for an improved and more quantitative modeling of the subsurface. In particular, the use of a 3D forward model allows us to reduce assumptions that mainly affect the quantitative σ results, and, furthermore allows us to simulate important details including borehole structure, borehole filling, and finite length antennas.

ACKNOWLEDGMENTS

The authors gratefully acknowledge the computing time granted by the John von Neumann Institute for Computing (NIC) and provided on the supercomputer JURECA at Jülich Supercomputing Centre (JSC). We thank Stewart Greenhalgh for helping us in the early stage of this study. We thank two anonymous reviewers, associate editor, assistant editor Colin Farquharson and editor in chief Jeffrey Shragge for suggestions and comments that helped us to improve the paper greatly.

References

Agudo, O. C., N. Vieira, M. Warner, J. Morgan, and I. C. London, 2016, Acoustic full-waveform inversion in an elastic world: SEG Technical Program Expanded Abstracts 2016, 1058–1062.

Allen Taflove, 1995, Computational Electrodynamics: The Finite-Difference Time-Domain Method: Artech House.

Annan, A. P., 2009, Chapter 1 - Electromagnetic Principles of Ground Penetrating Radar, *in* H. M. Jol, ed., Ground Penetrating Radar Theory and Applications, Elsevier, 1–40.

Auer, L., A. M. Nuber, S. A. Greenhalgh, H. Maurer, and S. Marelli, 2013, A critical appraisal of asymptotic 3D-to-2D data transformation in full-waveform seismic crosshole tomography: Geophysics, **78,** no. 6, R235–R247.

Belina, F. A., J. R. Ernst, and K. Holliger, 2009, Inversion of crosshole seismic data in heterogeneous environments: Comparison of waveform and ray-based approaches: Journal of Applied Geophysics, **68**, 85–94.

Berenger, J. P., 1994, A perfectly matched layer for the absorption of electromagnetic waves: Journal of Computational Physics, **114**, no. 2, 185–200.

Bleibinhaus, F., R. W. Lester, and J. A. Hole, 2009, Applying waveform inversion to wide-angle seismic surveys: Tectonophysics, **472**, 238–248.

Bleistein, N., 1986, Two and half dimension in-plane wave propagation: Geophysical Prospecting, **34**, 686–703.

Brenders, A. J., and R. G. Pratt, 2007, Full waveform tomography for lithospheric imaging: Results from a blind test in a realistic crustal model: Geophysical Journal International,

168, no. 1, 133–151.

Brossier, R., S. Operto, and J. Virieux, 2009, Seismic imaging of complex onshore structures by 2D elastic frequency-domain full-waveform inversion: Geophysics, **74**, no. 6, WCC105–WCC118.

Butzer, S., A. Kurzmann, and T. Bohlen, 2013, 3D elastic full-waveform inversion of small-scale heterogeneities in transmission geometry: Geophysical Prospecting, **61**, 1238–1251.

Červený V., 2001, Seismic Ray Theory: Cambridge University Press, 234-416.

Červený V., and I. Pšenčík, 2011, Seismic, Ray Theory, *in* H. K. Gupta, ed., Encyclopedia of Solid Earth Geophysics, Springer Netherlands, 1244–1258.

Chunduru, R. K., M. K. Sen, and P. L. Stoffa, 1997, Hybrid optimization methods for geophysical inversion: Geophysics, **62**, no. 4, 1196-1207.

Cirpka, O. a., M. N. Fienen, M. Hofer, E. Hoehn, A. Tessarini, R. Kipfer, and P. K. Kitanidis, 2007, Analyzing bank filtration by deconvoluting time series of electric conductivity: Ground Water, **45**,no. 3, 318–328.

Coscia, I., S. A. Greenhalgh, N. Linde, J. Doetsch, L. Marescot, T. Günther, T. Vogt, and A. G. Green, 2011, 3D crosshole ERT for aquifer characterization and monitoring of infiltrating river water: Geophysics, **76**, no. 2, G49–G59.

Crase, E., A. Pica, M. Noble, J. McDonald, and A. Tarantola, 1990, Robust elastic nonlinear waveform inversion: Application to real data: Geophysics, **55**, 527–538.

Dessa, J. X., and G. Pascal, 2003, Combined traveltime and frequency-domain seismic waveform inversion: A case study on multi-offset ultrasonic data: Geophysical Journal

International, **154**, 117–133.

Dickens, T. A., 1994, Diffraction tomography for crosswell imaging of nearly layered media: Geophysics, **59**, 694–706.

Diem, S., T. Vogt, and E. Hoehn, 2010, Räumliche Charakterisierung der hydraulischen Leitfähigkeit in alluvialen Schotter-Grundwasserleitern: Ein Methodenvergleich: Grundwasser, **15**, 241–251.

Doetsch, J., N. Linde, I. Coscia, S. A. Greenhalgh, and A. G. Green, 2010, Zonation for 3D aquifer characterization based on joint inversions of multimethod crosshole geophysical data: Geophysics, **75**, 53–64.

Dorn, C., N. Linde, T. Le Borgne, O. Bour, and L. Baron, 2011, Single-hole GPR reflection imaging of solute transport in a granitic aquifer: Geophysical Research Letters, **38**, 1–5.

Ernst, J. R., H. Maurer, A. G. Green, and K. Holliger, 2007a, Full-Waveform Inversion of Crosshole Radar Data Based on 2-D Finite-Difference Time-Domain Solutions of Maxwell ' s Equations: IEEE Transactions on Geoscience and Remote Sensing,, **45**, no. 9, 2807–2828.

Ernst, J. R., A. G. Green, H. Maurer, and K. Holliger, 2007b, Application of a new 2D time-domain full-waveform inversion scheme to crosshole radar data: Geophysics, **72**, no 5, J53.

Fichtner, A., 2011, Full Seismic Waveform Modelling and Inversion: Advances in Geophysical and Environmental Mechanics and Mathematics, 83–88.

Giannopoulos, A., 2005, Modelling ground penetrating radar by GprMax: Construction and Building Materials, **19**, 755–762.

Giannopoulos, A., 2012, Unsplit implementation of higher order PMLs: IEEE Transactions on Antennas and Propagation, **60**, 1479–1485.

Greenhalgh, S. A., B. Zhou, D. R. Pant, and A. Green, 2007, Numerical study of seismic scattering and waveguide excitation in faulted coal seams: Geophysical Prospecting, **55**, 185–198.

Gueting, N., T. Vienken, A. Klotzsche, J. van der Kruk, J. Vanderborght, J. Caers, H. Vereecken, and A. Englert, 2017, High resolution aquifer characterization using crosshole GPR full-waveform tomography: Comparison with direct-push and tracer test data: Water Resources Research, **53**, 49–72.

Hagness, S., and A. Taflove, 1997, Finite-Difference Time-Domain (FDTD) Computational Electrodynamics Simulations of Microlaser Cavities in One and Two Spatial Dimensions, *in* T. G. Campbell, R. A. Nicolaides, and M. D. Salas, eds., Computational Electromagnetics and Its Applications, Springer Netherlands, 229–251.

Hollender, F., S. Tillard, and L. Corin, 1999, Multifold borehole radar acquisition and processing: Geophysical Prospecting, **47**, 1077–1090.

Holliger, K., and H. R. Maurer, 2004, Effects of stochastic heterogeneity on ray-based tomographic inversion of crosshole georadar amplitude data: Journal of Applied Geophysics, **56**, no. 3, 177–193.

Holliger, K., M. Musil, and H. R. Maurer, 2001, Ray-based amplitude tomography for crosshole georadar data: A numerical assessment: Journal of Applied Geophysics, **47**, 285–298.

Hubbard, S. S., J. E. Peterson, E. L. Majer, P. T. Zawislanski, K. H. Williams, J. Roberts, and F. Wobber, 1997, Estimation of permeable pathways and water content using tomographic radar data: The Leading Edge, **16**, 1623–1630.

Keskinen, J., A. Klotzsche, M. C. Looms, J. Moreau, J. van der Kruk, K. Holliger, L. Stemmerik, and L. Nielsen, 2017, Full-waveform inversion of Crosshole GPR data: Implications for porosity estimation in chalk: Journal of Applied Geophysics, **140**, 102–116.

Klotzsche, A., H. Vereecken, and J. van der Kruk, 2019, Review of Crosshole GPR Full-waveform Inversion of Experimental Data: Recent Developments, Challenges and Pitfalls: Geophysics, **84**, no. 6, H13-H28.

Klotzsche, A., J. van der Kruk, J. Bradford, and H. Vereeken, 2014, Detection of spatially limited high-porosity layers using crosshole GPR signal analysis and full-waveform inversion: Water Resources Research, **50**, 6966–6985.

Klotzsche, A., J. van der Kruk, G. Meles, and H. Vereecken, 2012, Crosshole GPR full-waveform inversion of waveguides acting as preferential flow paths within aquifer systems: Geophysics, **77**, no. 4, H57.

Klotzsche, A., J. Jan van der, Kruk, L. Niklas, J. Doetsch, and H. Vereecken, 2013, 3-D characterization of high-permeability zones in a gravel aquifer using 2-D crosshole GPR full-waveform inversion and waveguide detection: Geophysical Journal International, **195**, 932–944.

Klotzsche, A., J. van der Kruk, G. A. Meles, J. Doetsch, H. Maurer, and N. Linde, 2010, Full-waveform inversion of cross-hole ground-penetrating radar data to characterize a gravel aquifer close to the Thur River, Switzerland: Near Surface Geophysics, **8**, 635–649.

Krause, D., and P. Thörnig, 2016, JURECA: General-purpose supercomputer at Jülich Supercomputing Centre: Journal of Large-Scale Research Facilities JLSRF, **2**, A62.

Kuroda, S., M. Takeuchi, and H. J. Kim, 2007, Full-waveform inversion algorithm for interpreting crosshole radar data: A theoretical approach: Geosciences Journal, **11**, 211–217.

Lavoué, F., R. Brossier, S. Garambois, J. Virieux, and L. Metivier, 2013, 2D full waveform inversion of GPR surface data: Permittivity and conductivity imaging: IWAGPR 2013 - Proceedings of the 2013 7th International Workshop on Advanced Ground Penetrating Radar, **1**.

Lavoué, F., R. Brossier, L. Métivier, S. Garambois, and J. Virieux, 2014, Two-dimensional permittivity and conductivity imaging by full waveform inversion of multioffset GPR data: A frequency-domain quasi-Newton approach: Geophysical Journal International, **197**, no. 1, 248–268.

Looms, M. C., K. H. Jensen, A. Binley, and L. Nielsen, 2008, Monitoring Unsaturated Flow and Transport Using Cross-Borehole Geophysical Methods: Vadose Zone Journal, **7**, 227.

Looms, M. C., A. Klotzsche, J. van der Kruk, T. H. Larsen, A. Edsen, N. Tuxen, N. Hamburger, J. Keskinen, and L. Nielsen, 2018, Mapping sand layers in clayey till using crosshole ground-penetrating radar: Geophysics, **83**,no. 1, A21–A26.

Maurer, H., and M. Musil, 2004, Effects and removal of systematic errors in crosshole georadar attenuation tomography: Journal of Applied Geophysics, **55**, no. 3-4, 261–270.

Meles, G. A., J. van der Kruk, S. A. Greenhalgh, J. R. Ernst, H. Maurer, and A. G. Green, 2010, A new vector waveform inversion algorithm for simultaneous updating of conductivity and permittivity parameters from combination crosshole/borehole-to-surface GPR data: IEEE Transactions on Geoscience and Remote Sensing, **48**, no. 9, 3391–3407.

Miksat, J., T. M. Müller, and F. Wenzel, 2008, Simulating three-dimensional seismograms in 2.5-dimensional structures by combining two-dimensional finite difference modelling and ray tracing: Geophysical Journal International, **174**, no. 1, 309–315.

Mozaffari, A., A. Klotzsche, G. He, C. Warren, A. Giannopoulos, H. Vereecken, and J. Van Der Kruk, 2016, Towards 3D full-waveform inversion of crosshole GPR data: 2016 16th International Conference on Ground Penetrating Radar (GPR), 1-4.

Mulder, W. A., C. Perkins, and M. J. Van De Rijzen, 2010, 2D Acoustic Full Waveform Inversion of a Land Seismic Line: Eage, 14–17.

Pratt, R. G., 1999, Seismic waveform inversion in the frequency domain, Part 1: Theory and verification in a physical scale model: Geophysics, **64**, no. 2, 888-901.

Pratt, R. G., and R. M. Shipp, 1999, Seismic waveform inversion in the frequency domain; Part 2; Fault delineation in sediments using crosshole data: Geophysics, **64**, no. 3, 902–914.

Pratt, R. G., C. Shin, and G. J. Hicks, 1998, Gauss-Newton and full Newton methods in frequency-space seismic waveform inversion: Geophysical Journal International, **133**, no. 2, 341–362.

Rector, J. W., and J. K. Washbourne, 1994, Characterization of resolution and uniqueness in crosswell direct-arrival traveltime tomography using the Fourier projection slice theorem: Geophysics, **59**, no. 11, 1642–1649.

Sirgue, L., J. Etgen, and U. Albertin, 2008, 3D frequency domain waveform inversion using time domain finite difference methods: 70th EAGE Conference & Exhibition, 9–12.

Slater, L., M. D. Zaidman, M. D. Binley, and L. J. West, 1997, Electrical imaging of saline tracer migration for the investigation of unsaturated zone transport mechanisms: Hydrology and Earth System Sciences, **1**, no. 2, 291-302.

Song, Z., and P. R. Williamson, 1995, Frequency-domain acoustic-wave modeling and inversion of crosshole data: Part I—2.5-D modeling method: , Geophysics, **60**, no. 3, 784–795.

Stratton, J. A., 2015, The Magnetostatic Field: In Electromagnetic Theory, 225-267.

Streich, R., and J. van der Kruk, 2007, Characterizing a GPR antenna system by near-field electric field measurements: Geophysics, **72**, no. 5, A51-A55.

Tabarovsky, L. A., and M. B. Rabinovich, 1996, 2 . 5-D Modeling in electromagnetic: Applied Geophysics, **35**, no. 4, 261–284.

Tarantola, A., 1984, Inversion of seismic reflection data in the Acoustic Approximation: Geophysics, **49**, no. 8, 1259–1266.

Tarantola, A., 1986, A strategy for nonlinear elastic inversion of seismic reflection data: Geophysics, **51**, no. 10, 1893.

Tronicke, J., and K. Holliger, 2004, Short Note Effects of gas- and water-filled boreholes on the amplitudes of crosshole georadar data as inferred from experimental evidence: Geophysics, **69**, no. 5, 1255–1260.

Virieux, J., and S. Operto, 2009, An overview of full-waveform inversion in exploration geophysics: Geophysics , **74**, no. 6, WCC1–WCC26.

Van Vorst, D. G., M. J. Yedlin, J. Virieux, and E. S. Krebes, 2014, Three-dimensional to two-dimensional data conversion for electromagnetic wave propagation using an acoustic transfer function: application to cross-hole GPR data: Geophysical Journal International, **198**, no. 1, 474–483.

Warner, M., A. Ratcliffe, T. Nangoo, J. Morgan, A. Umpleby, N. Shah, V. Vinje, I. Štekl, L. Guasch, C. Win, G. Conroy, and A. Bertrand, 2013, Anisotropic 3D full-waveform inversion: Geophysics, **78**, no. 2, R59–R80.

Warren, C., and A. Giannopoulos, 2011, Creating finite-difference time-domain models of commercial ground-penetrating radar antennas using Taguchi's optimization method: Geophysics, **76**, no. 2, G37–G47.

Warren, C., A. Giannopoulos, and I. Giannakis, 2016, gprMax: Open source software to simulate electromagnetic wave propagation for Ground Penetrating Radar: Computer Physics Communications, **209**, 163–170.

Watson, F., 2016, Towards 3D full-wave inversion for GPR: 2016 IEEE Radar Conference, RadarConf 2016.

Williamson, P. R., 1991, A guide to the limits of resolution imposed by scattering in ray tomography: Geophysics, **56**, no. 2, 202-207.

Williamson, P. R., and R. G. Pratt, 1995, A critical review of acoustic wave modeling procedures in 2.5 dimensions: Geophysics, **60**, no. 2, 591-595.

Wu, R., and M. N. Toksöz, 1987, Diffraction tomography and multisource holography applied to seismic imaging: Geophysics, **52**, no. 1, 11–25.

Table Caption:

Table 1. Results of the synthetic study using different inversion strategies and different starting models *SM.* Maximum lateral average error *LAE* and average error *AE* for the entire domain between the boreholes for ε_r and σ. Computation time *CT*, reduction of the computational time, and RMS reduction normalized to the starting models (SM represented by 100%) for 2D and 2.5D FWI. The bold values indicate the best results.

Figures Captions:

Figure 1. Synthetic subsurface crosshole GPR setup with: model a) homogenous medium (ε_r = *12*) (1a); model b) homogenous medium (ε_r = *18*) (1d); model c) homogenous medium (ε_r = *12*) with a waveguide structure (ε_r = *18*) in the center (1g); and model d) homogenous medium (ε_r = *12*) with a waveguide structure (ε_r = *18*) in the center with an unsaturated zone (ε_r = 5) on top (1j). The transmitter-receiver pairs are marked by red crosses. The corresponding simulated 2D, calculated semi-2D, and 3D traces are in the center column, where the major events are assigned to possible ray paths by number and dashed purple circles. The frequency spectra are presented in the right column. Note that the amplitude of the semi-2D and 3D traces are scaled by the ratio of $A_{max}^{2D}/\ A_{max}^{semi-2D}$.

Figure 2. Relative dielectric permittivity (a) and electrical conductivity (b) models based on Klotzsche et al. (2012) as the simulated reality for synthetic analysis. Note the logarithmic scale for the σ tomogram. Transmitter and receiver positions are indicated by circle and crosses, respectively.

Figure 3. ε_r and σ models for 2D (a and b) and 2.5D FWI (c and d), and corresponding lateral average errors plotted on the left side of the tomograms. A-A and B-B show the positions of the cross-sections presented in Figure 4. Note the logarithmic scale for σ tomograms. Transmitter and receiver positions are indicated by circle and crosses, respectively.

Figure 4. ε_r and σ values of the cross-sections A-A (a and b) and B-B (c and d) (position shown by dotted line in Figure 3) for the reference values (blue), and models produced with 2D (red) and 2.5D FWI (black).

Figure 5. ε_r and σ and tomograms produced by 2.5D FWI for different starting models created from the 1st (a and b), 4th (c and d) and 7th (e and f) iteration of 2D FWI. Corresponding lateral

average errors are plotted on the right side of each tomogram. Note the logarithmic scale for σ tomograms. Transmitter and receiver positions are indicated by circle and crosses, respectively.

Figure 6. Updated ε_r starting model (a), ε_r, (b) and σ (c) resulting tomograms of the 2.5D FWI and the corresponding lateral average model errors on the left side. Note the logarithmic scale for σ tomogram. Transmitter and receiver positions are indicated by circle and crosses, respectively.

Figure 7. RMS misfit curves for 2D FWI (blue) and 2.5D FWI (red) using the same starting models, and, the 2.5D FWI using the updated ε_r starting model. RMS curves are normalized to the starting model value (0 iteration) used for the 2D and 2.5D FWI.

Figure 8. Comparison of the 2D effective source wavelet based on Klotzsche et al. (2012) in red and the 2.5D effective source wavelet in blue using the deconvolution approach. Note both wavelets are normalized to their maximum amplitude.

Figure 9. 2.5D FWI tomograms for ε_r (a) and σ (b) for the experimental data of the Widen test site using the updated starting model (see Figure 6a) and effective source wavelet (see Figure 8, blue). Note the logarithmic scale for σ tomogram. Transmitter and receiver locations are indicated by circles and crosses, respectively.

Table 1. Results of the synthetic study using different inversion strategies and different starting models *SM.* Maximum lateral average error *LAE* and average error *AE* for the entire domain between the boreholes for ε_r and σ. Computation time *CT*, reduction of the computational time, and RMS reduction normalized to the starting models (SM represented by 100%) for 2D and 2.5D FWI. The bold values indicate the best results.

FWI strategy	Max. *LAE* (%) for ε_r	*AE* (%) of ε_r	Max.*LAE* (%) for σ	*AE* (%) for σ	CT for 20 iteration (min)	CT reduction compare to 2.5D FWI (%)	RMS reduction normalized to SM (%)
2D	25	2.5	35	2.8	4,5	-	78
2.5D	6	0.18	19	0.5	1196.7	-	88
2.5D – with 1st iteration of the 2D FWI as SM	8	0.21	19	1.0	1136.4	5	84
2.5D – with 4th iteration of the 2D FWI as SM	19	1.55	28	1.6	957.7	20	82
2.5D – with 7th iteration of	23	1.9	33	2.2	778.9	35	81

the 2D FWI as SM							
2.5D with updated SM	**8**	**0.16**	**11**	**0.45**	**664.8**	**44**	**88**

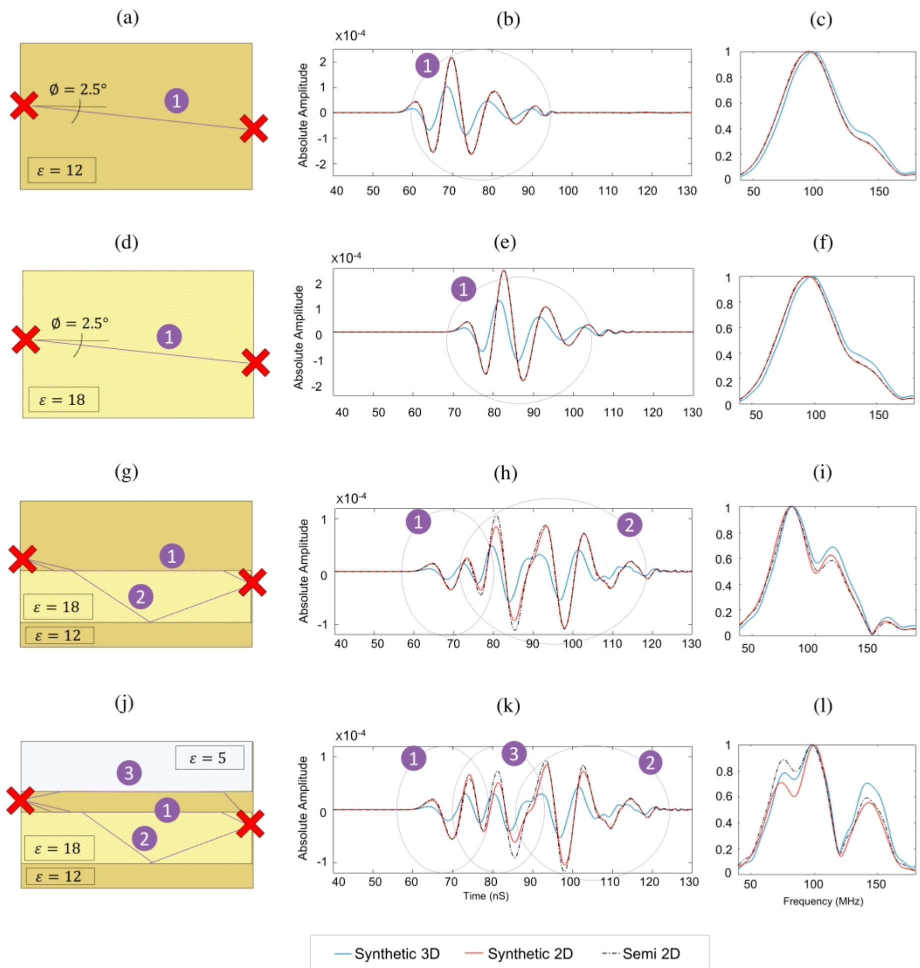

Figure 1 / Synthetic subsurface crosshole GPR setup with: model a) homogenous medium (εr = 12) (1a); model b) homogenous medium (εr = 18) (1d); model c) homogenous medium (εr = 12) with a waveguide structure (εr = 18) in the center (1g); and model d) homogenous medium (εr = 12) with a waveguide structure (εr = 18) in the center with an unsaturated zone (εr = 5) on top (1j). The transmitter-receiver pairs are marked by red crosses. The corresponding simulated 2D, calculated semi-2D, and 3D traces are in the center column, where the major events are assigned to possible ray paths by number and dashed purple circles. The frequency spectra are presented in the right column. Note that the amplitude of the semi-2D and 3D traces are scaled by the ratio of A_{max}^{2D}/ $A_{max}^{semi\text{-}2D}$.

467x481mm (300 x 300 DPI)

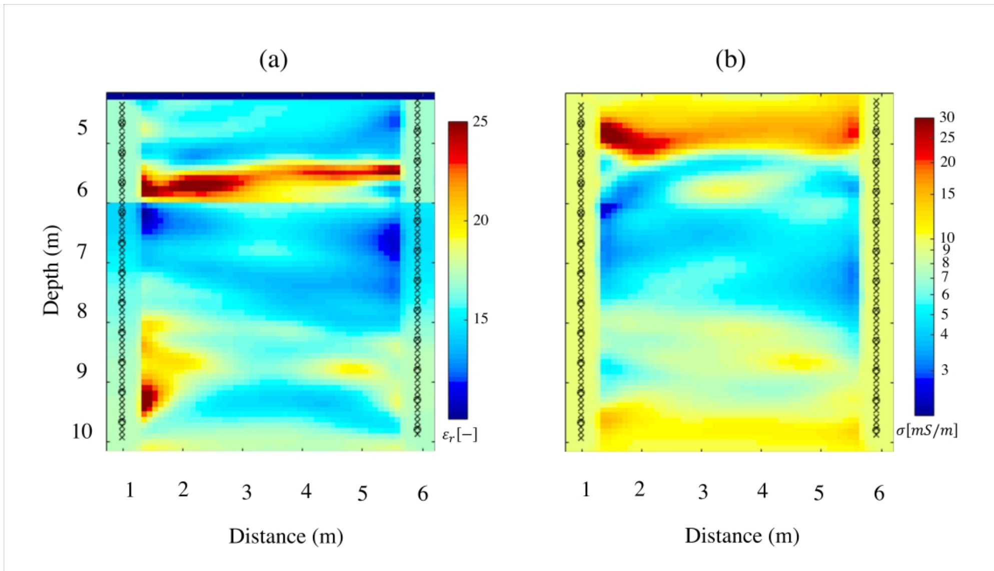

Figure 2 / Relative dielectric permittivity (a) and electrical conductivity (b) models based on Klotzsche et al. (2012) as the simulated reality for synthetic analysis. Note the logarithmic scale for the σ tomogram. Transmitter and receiver positions are indicated by circle and crosses, respectively.

628x361mm (300 x 300 DPI)

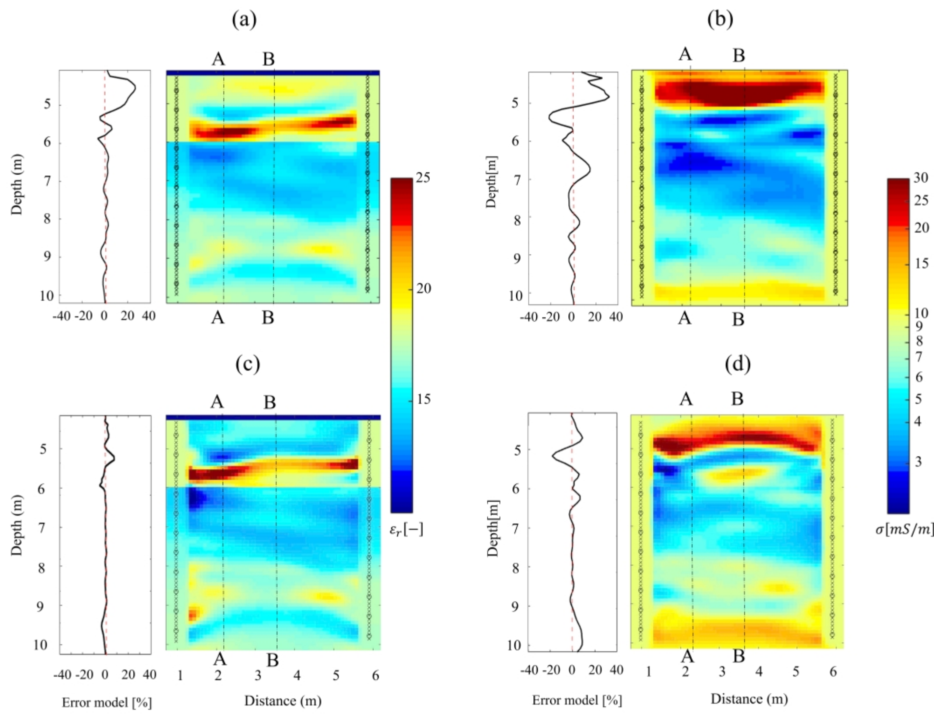

Caption : Figure 3 / εr and σ models for 2D (a and b) and 2.5D FWI (c and d), and corresponding lateral average errors plotted on the left side of the tomograms. A-A and B-B show the positions of the cross-sections presented in Figure 4. Note the logarithmic scale for σ tomograms. Transmitter and receiver positions are indicated by circle and crosses, respectively.

558x448mm (300 x 300 DPI)

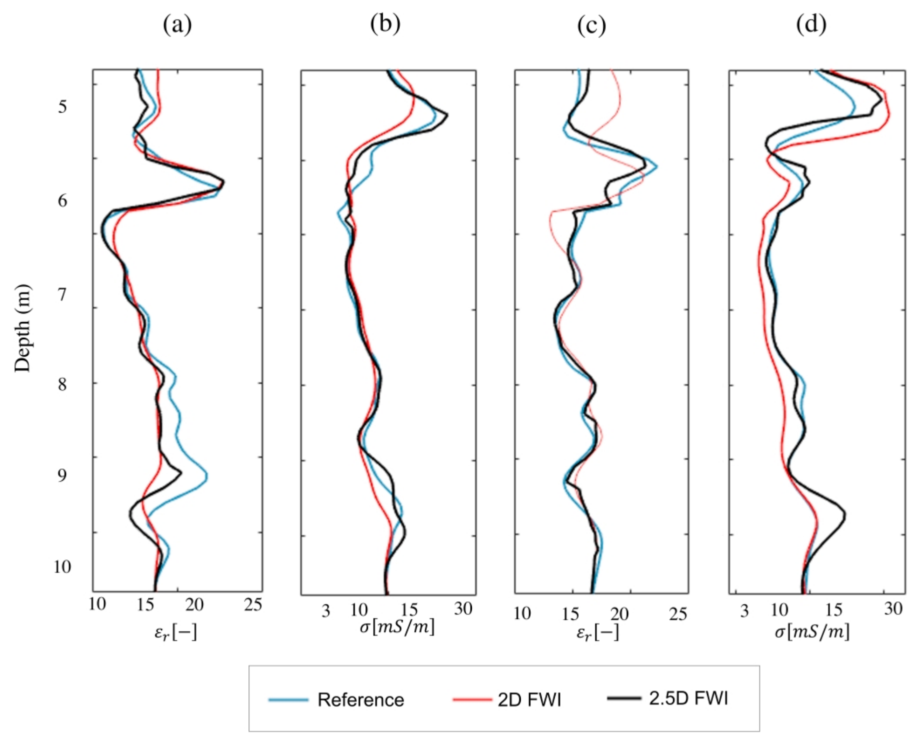

Figure 4 / εr and σ values of the cross-sections A-A (a and b) and B-B (c and d) (position shown by dotted line in Figure 3) for the reference values (blue), and models produced with 2D (red) and 2.5D FWI (black).

516x409mm (300 x 300 DPI)

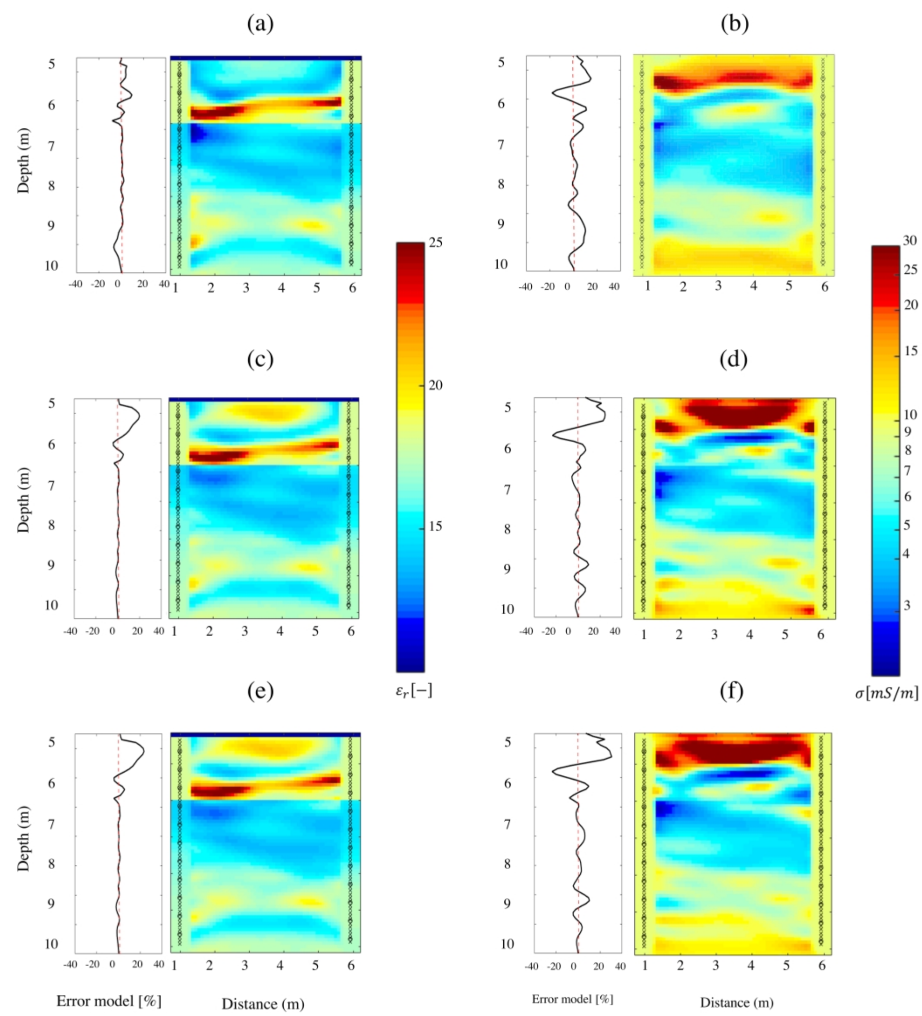

Figure 5 / εr and σ and tomograms produced by 2.5D FWI for different starting models created from the 1st (a and b), 4th (c and d) and 7th (e and f) iteration of 2D FWI. Corresponding lateral average errors are plotted on the right side of each tomogram. Note the logarithmic scale for σ tomograms. Transmitter and receiver positions are indicated by circle and crosses, respectively.

392x425mm (300 x 300 DPI)

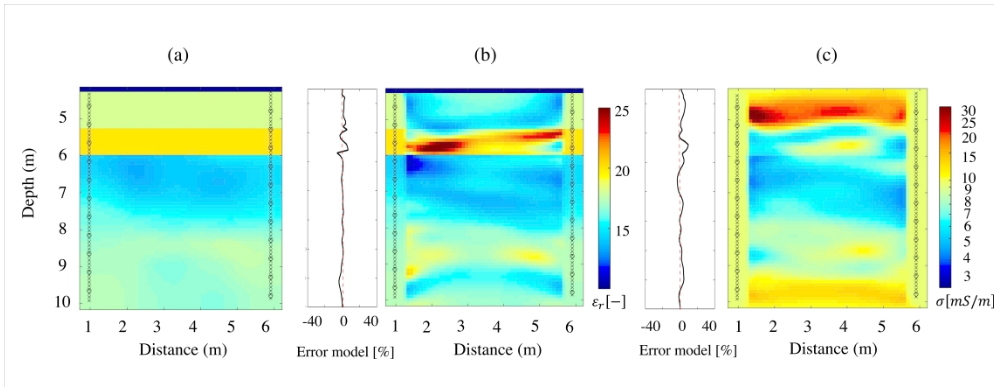

Figure 6 / Updated εr starting model (a), εr, (b) and σ (c) resulting tomograms of the 2.5D FWI and the corresponding lateral average model errors on the left side. Note the logarithmic scale for σ tomogram. Transmitter and receiver positions are indicated by circle and crosses, respectively.

652x253mm (300 x 300 DPI)

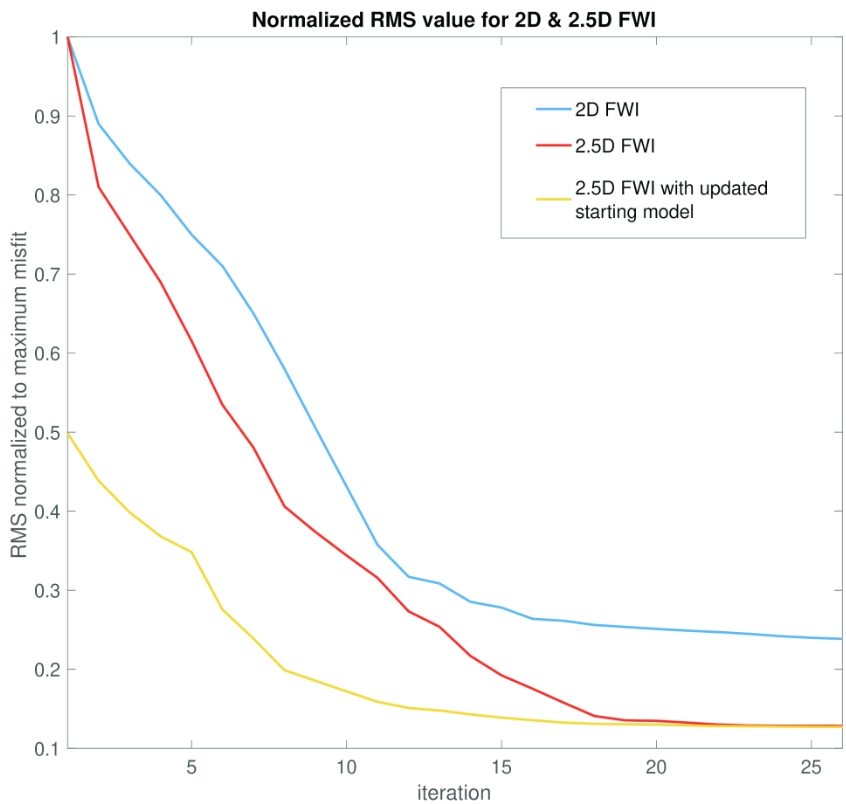

Figure 7 / RMS misfit curves for 2D FWI (blue) and 2.5D FWI (red) using the same starting models, and, the 2.5D FWI using the updated εr starting model. RMS curves are normalized to the starting model value (0 iteration) used for the 2D and 2.5D FWI.

297x260mm (300 x 300 DPI)

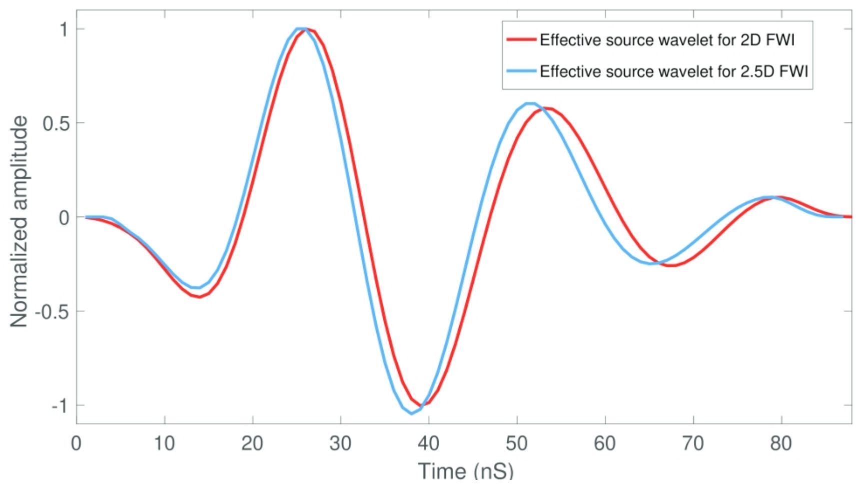

Figure 8 / Comparison of the 2D effective source wavelet based on Klotzsche et al. (2012) in red and the 2.5D effective source wavelet in blue using the deconvolution approach. Note both wavelets are normalized to their maximum amplitude.

351x178mm (300 x 300 DPI)

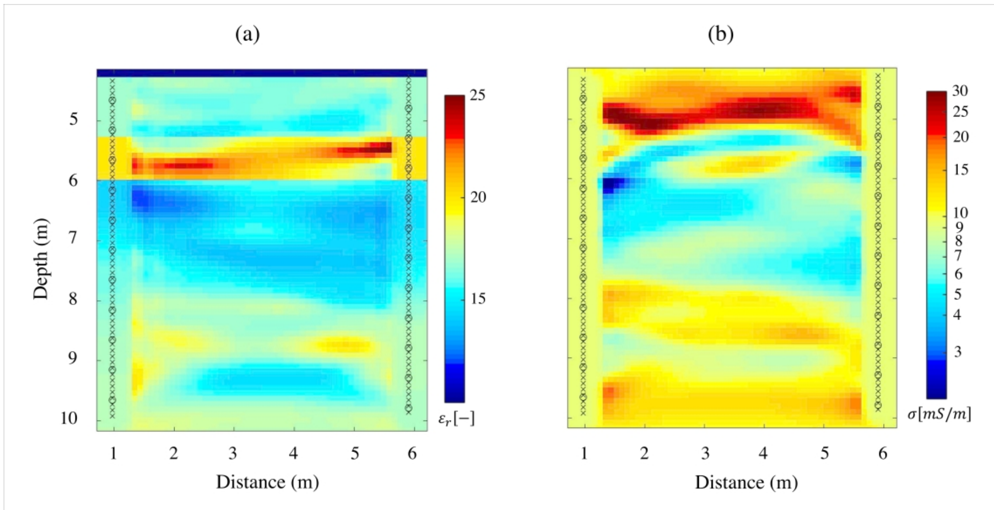

Figure 9 / 2.5D FWI tomograms for εr (a) and σ (b) for the experimental data of the Widen test site using the updated starting model (see Figure 6a) and effective source wavelet (see Figure 8, blue). Note the logarithmic scale for σ tomogram. Transmitter and receiver locations are indicated by circles and crosses, respectively.

638x327mm (300 x 300 DPI)